Luminescence Properties of Al2O3:Ti in the Blue and Red Regions: A Combined Theoretical and Experimental Study

Théo Cavignac, Maxence Vigier, Emmanuel Fritsch, Philippe Deniard, Stéphane Jobic, Camille Latouche

Luminescence properties of Al_2O_3:Ti in the blue and red regions: a combined theoretical and experimental study

Théo Cavignac,[†] Maxence Vigier,[†] Emmanuel Fritsch,[†] Philippe Deniard,[†] Stéphane Jobic,[*,†] and Camille Latouche[*,†,‡]

†*Nantes Université, CNRS, Institut des Matériaux de Nantes Jean Rouxel, IMN, F-44000 Nantes*

‡*Institut Universitaire de France (IUF), Paris F-75005, France*

E-mail: stephane.jobic@cnrs-imn.fr; camille.latouche@cnrs-imn.fr

Abstract

Using on jointly experimental results and first-principles calculations, we unambiguously assign the underlying mechanisms behind two commonly observed luminescence bands for the Al_2O_3 material. Indeed, we show that the red band is associated with a Ti^{3+} *d-d* transitions as expected, while the blue band is the combination of the Ti^{3+} + O^- → Ti^{4+} + O^{2-} and $V_O^{\bullet} + e^- \rightarrow V_O^{\times}$ deexcitation processes. Thanks to our last developments which take into account the vibrational contributions to the electronic transitions in solids, we were able to simulate the luminescence spectra for the different signatures. The excellent agreement with experiment demonstrates that it should be possible to predict the color of the material with a CIE chromaticity diagram. We also anticipated the luminescence signature of Al_2O_3 :Ti,Ca and Al_2O_3 :Ti,Be that were confirmed by experiment.

Introduction

Aluminum oxide (Al_2O_3) is recognized for its exceptional versatility and resilience, attributed to a unique combination of properties. With a melting point of 2072 degrees Celsius, significantly surpassing that of most metals and ceramics, it is a preferred material for high-temperature applications. A hardness rating of 9 on the Mohs scale endows it with remarkable resistance to wear. Its low electrical conductivity qualifies it as an effective insulator, complemented by superior wear resistance, ensuring durability in demanding environments. Noteworthy is its unwavering chemical stability, guaranteeing structural integrity even in the presence of harsh chemicals and extreme conditions. These distinctive properties establish Al_2O_3 as a prominent and widely utilized material.[1–12]

The natural form of alumina (α-Al_2O_3), called corundum, is also known for its optical properties. Intrinsically colorless due to a very large band gap ($\approx$ 9 eV), the presence of numerous «extrinsic» impurities (in a lesser extent intrinsic one) may lead to the appearance of absorption bands in the visible range.[13] Thus, the hue of Al_2O_3 could range from blue thanks to a $Fe^{2+} + Ti^{4+} \rightarrow Fe^{3+} + Ti^{3+}$ to red or green in presence of Cr^{3+} due to on-site *d*–*d* transition.[14,15] Many samples have also been described as luminescent, in that case the origin of the observed emissions being related to intrinsic and extrinsic defects.[2,16,17]

Among all the dopants, Al_2O_3 may naturally contain titanium, and the intense evolution of alumina doping techniques has led to the creation of lasers labeled Al_2O_3:Ti.[18–20] In that case, a luminescence band appears between 700 and 770 nm (*i.e.* 1.77 and 1.61 eV) and is unambiguously assigned to a Ti^{3+} *d*-*d* on-site transition.[21–24]

A second band in the blue region, with a maximum around 430 nm (2.88 eV), has also been observed in Ti-based laser.[16] Unlike the red one, this luminescence generated many theories but no definitive proof has yet been established to certify its origin(s). Indeed, this emission was successively assigned to the presence of F centers (a neutral defect made of an oxygen vacancy with two trapped electrons), to Ti^{4+} with a possible presence of a +II cation (*e.g.* Mg^{2+}).[22,25–45]

However, despite numerous studies, the origin of the blue luminescence band is still uncertain. It is at this point that theoretical calculations must play a pivotal role. Nevertheless, despite the intense development of new theoretical calculation techniques, one could not fully assess the Ti-related luminescence properties in Al_2O_3 so far, even though some electronic transitions (through defect formation enthalpies computations) and defect formation energies are known.[46–57] The luminescence properties are still challenging to model and up to now nobody succeeded in simulating simultaneously the red and the blue luminescence signatures with a good accuracy. In this article, we draw upon recent computational techniques that we have developed with the aim of simulating luminescence. Indeed, we were able (i) to get insights of the structure of the excited state (ES) and to get the luminescence energy of the ZrO_2:Ti material,[58] and (ii) to simulate the full luminescence spectrum including the vibrational contributions to the electronic transition of $BaZrO_3$:Ti.[59] Herein, we simulated both aforementioned luminescence signatures, *i.e.* the red one from Ti^{3+} and the blue one, which was still under debate. In this paper, we provide a definitive answer concerning the origin of the observed blue band thanks to state-of-the-art modeling in solids. Moreover, our model predicts the fine tuning of the blue luminescence band depending on the +II charge compensating cation, which was subsequently confirmed using chemical syntheses and characterizations.

Methods

Experimental details

Luminescence spectra were collected on five distinct Al_2O_3:Ti samples:

- one synthetic Verneuil monocrystal (hereafter labeled **I**) was purchased from the company Djevahirdjian scientific stones (Switzerland),
- one natural gemstone (hereafter labeled **II**) from Sri Lanka was acquired through Astrid

Corporation (Hong Kong),

- one synthetic powder sample with Ti+Mg codoping (hereafter labeled **III**) was prepared for this study (see SI for details),
- one synthetic powder sample with Ti+Ca codoping (hereafter labeled **IV**) was prepared for this study,
- one natural sample (hereafter labeled **V**) treated with Be diffusion technique also purchased to Astrid Corporation (Hong Kong).[60]

Traces elements were identified and quantified for all samples via LA-ICP-MS analyses (see SI). Major detected elements are summed up in Table 1.

Table 1: ICP-MS elemental analysis on natural and synthetic Al_2O_3 samples. *bld* stands for below limits of detection.

	^{47}Ti (ppm)	^{24}Mg (ppm)	^{9}Be (ppm)	^{44}Ca (ppm)
I	468	5	*bld*	*bld*
II	305	118	*bld*	*bld*
III	3910	1822	1	*bld*
IV	3085	525	*bld*	8462
V	114	556	1437	1647

The spectroscopic data were acquired with a Horiba JobinYvon Fluorolog-3 fluorimeter. The collect of emission spectra were carried out in the 300 to 900 nm range (1.37 to 4.13 eV) with an excitation at 254 nm. For Raman spectrum recording, an ultrapure sample Al_2O_3 (hereafter labeled **VI**) loaned from Daniel Ritz at Spolchemie (Czech Republic) was used. Raman scattering spectra were obtained on a Jobin Yvon T64000 spectrometer with a 514 nm Ar-laser (see SI).

Computational details

Structures and electronic structures of the ground and excited states computations were performed with the plane wave software VASP with the GGA functional PBE, using the

projector augmented wave formalism and a cutoff energy of 550 eV.[61–64] For the vibrational properties, the CRYSTAL17 software was used with the global hybrid PBE0 functional for the bulk, and the PBE functional for the faulted cell, together with the DZVP Rev2 basis set after a proper geometrical relaxation.[65–67]

Bulk computations The host structure was studied on the 10 atoms primitive cell (rhombohedral setting of the regular $R\bar{3}c$ trigonal cell with Z = 2). For the structural relaxation, the first Brillouin zone was paved of a $10 \times 10 \times 10$ k-mesh Monkhorst-Pack grid and forces were optimized under $5.0 \cdot 10^{-3}$ eV/Å. For accurate energy computations, the Brillouin zone was paved of a $13 \times 13 \times 13$ k-mesh Γ-centered grid and the residual of total energy was converged under 10^{-7} eV. For the vibrational computation, 5761 k-points and a convergence on the energy of 10^{-10} eV were used.

Al_2O_3:V_O and Al_2O_3:Ti(,M) ground and excited states (M= Mg, Ca and Be) The doped and co-doped Al_2O_3 were investigated using supercells of 120 atoms ($2 \times 2 \times 1$ with respect to the conventional trigonal cell). For these structures, only the atomic positions were allowed to relax, the volume being kept identical to the pure material in order to model diluted defect. Forces and energies were converged under 10^{-2} eV/Å and under 10^{-7} eV, respectively providing the coordinates and energy in the electronic ground state (point **A** from Figure 1). Excited state structures were relaxed using the so-called constrained DFT (cDFT) which allows one to specify an arbitrary electronic occupation of Kohn-Sham bands. The relaxation and energy computation with cDFT yields the energy and atomic positions of the most stabilized electronic state in the excited configuration (point **C** of Figure 1). These atomic positions are then used unrelaxed to compute the energy of point **D**. The energy difference between **C** and **D** is used here as the Electronic Vertical Transition energy. This method has already been used successfully in a previous study dealing with the luminescence properties of ZrO_2 and $BaZrO_3$ doped with titanium.[58,59] It is also a very well-known method in molecular simulation, which allows one to accurately predict the luminescence color of

transition metal complexes and molecular clusters.[68–70]

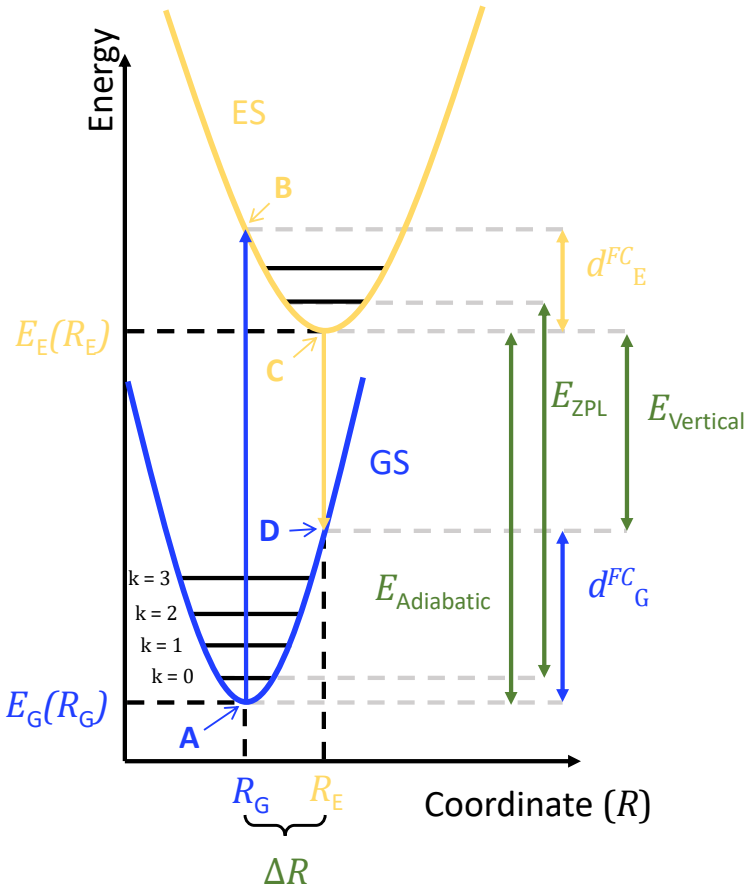

Figure 1: Schematic representation of the luminescence process with characteristic points. R_G is the position obtained from relaxing the GS. R_E is the position obtained from relaxing the ES. Point **A** is the electronic ground state, point **B** is the electronic excited state at the ground state position. Point **C** is the relaxed excited state, point **D** is the result of a vertical transition from point **C**. d_G^{FC} and d_E^{FC} are the Franck-Condon shifts. The Adiabatic Energy is used to approximate the Zero-Phonon-Line energy by neglecting the Zero-Point Energies (minimal vibrational energies in relaxed configurations)

Vibrationally resolved luminescence spectra For each electronic transition considered, a vibrationally resolved spectrum is computed. The method detailed in our previous work[59] is based on the quantum harmonic oscillator model. Essentially, it consists in what is called Adiabatic Shift in the molecular community.[71–74] In a multi-dimensional approach

(nD), it considers a distinct harmonic oscillator i for every vibrational mode of the GS. All transitions from the lowest vibrational state of the excited state, $|E, 0_1, \ldots, 0_n\rangle$, to any vibrationally excited ground state $|G, k_1, \ldots, k_n\rangle$ ($\forall i, k_i \in \mathbb{N}$) are considered. The intensity of each of these transitions is computed in the approximation that the dipole transition moment is independent of the vibrations and positions (Franck-Condon approximation).[75] As a consequence we discard the small linear dependency of the transition dipole on the displacement (the so called Hertzberg-Teller coupling). It results in a sum of contributions of the form:

$$L(\omega) = \sum_{k_1=1}^{+\infty} \ldots \sum_{k_n=1}^{+\infty} |\langle 0_1, \ldots, 0_n | k_1, \ldots, k_n \rangle|^2 \delta \left(\omega - E_{\mathrm{ZPL}} + \sum_{i=1}^{n} k_i \hbar \omega_i \right) \tag{1}$$

E_{ZPL}, the Zero-Phonon-Line energy, requires the knowledge of the ES Zero-Point Energy. Unfortunately, this quantity requires the knowledge of all ES vibrational modes which is very difficult to obtain in the solid state. We instead assume that the Zero-Point energy of GS and ES are similar and thus use $E_{\mathrm{Adiabatic}}$ to approximate E_{ZPL}. Furthermore, the overlap of ES and GS modes are computed under the approximation that ES vibrational modes are homothetic to the GS ones. This approach has already been used for the solid in some of our previous work:[59]

$$L(\omega) = \sum_{k_1,\ldots,k_n} \left(\prod_{i=1}^{n} |\langle 0 | k_i \rangle|^2 \right) \delta \left(\omega - E_{\mathrm{ZPL}} + \sum_{i=1}^{n} k_i \hbar \omega_i \right) \tag{2}$$

This expression can be rewritten into a more tractable form through a generative function approach, as shown in the seminal work of Kubo.[76] It implicates the computation of the mode specific Huang-Rhys factors S_i that are used in the evaluation of the $|\langle k_i | 0_i \rangle|^2$ terms. The Huang-Rhys factor for mode i is defined here by $S_i = \frac{d_{G,i}^{\mathrm{FC}}}{\hbar \omega_i} = \frac{1}{2} \omega_i \mu_i \Delta R_i$ where μ_i is the effective mass of mode i and ΔR_i is the displacement from R_E to R_G in the direction of the eigendisplacement of mode i.[77] S_i relates to the average quantum number of the i phonon and is larger when the vibronic coupling is stronger in this direction.

The result of Equation 2 is a discrete spectrum made of many peaks with no width. The discrete spectrum is then convoluted with a Gaussian lineshape to obtain the final spectrum. To obtain the full-width-at-half-maximum of the lineshape, we use a semi-classical model of the width of the total band.[78] In this model, the width of the band is obtained from the dispersion of the first vibrational wavefunction of ES multiplied by the gradient of the GS PES (see SI for details). This method's applicability relies on a strong vibronic coupling, and a near continuum in the GS vibrational states. As a result, it proves beneficial for analyzing broad, unstructured bands.

It is yet impossible to evaluate the full ES PES. Consequently, more approximations are required. The simplest approximation would be to assume the equivalence of ES and GS PES. This would, however, systematically underestimate the dispersion because the modes associated with larger displacement are likely to have significantly smaller frequencies in ES than in GS. Yet, these modes are the ones contributing the most to the width of the final band. As an alternative, we chose to approximate the ES PES with a single frequency computed by finite difference in the direction of the GS gradient. This provides an effective frequency that is most representative of the most coupled modes. This model enables a first order accounting of the effect of the temperature on the band shape through the consideration of a Bose-Einstein population of ES vibrational states. This temperature dependent total width is used to predict a linewidth for our simulation.

For practical reasons, phonons required by this procedure are computed with the software CRYSTAL17.[65,79] The PBE functional is used in order to be coherent with the positions obtained in previous computations.

To quantitatively qualify the localization of modes, we use a descriptor defined by Bell and collaborators[80] named the participation ratio. The participation ratio p represents the fraction of active atoms in the supercell for a given mode and is computed as follows:

$$p_i = \frac{N_{\text{eff}}}{N} = \frac{1}{N \sum_\alpha ||\gamma_{i,\alpha}||^2} \tag{3}$$

$\gamma_{i,\alpha}$ being the 3D vector representing the contribution of atom α to the eigenvector i.

An in-house (soon to be open-sourced) Python package is used to perform all the post-treatments.

Results and discussions

Photoluminescence experimental spectra

The collected photoluminescence spectra at room temperature of samples **I**, **II** and **III** are shown in Figure 2. Only sample **I** exhibits the red band that we are interested in. The blue band is positioned at slightly different energies for **I**, **II** and **III**, emissions peaking at 2.98 eV (416 nm), 2.93 eV (423 nm) and 2.83 eV (437 nm) respectively. Simulations will explain this variation (*vide infra*).

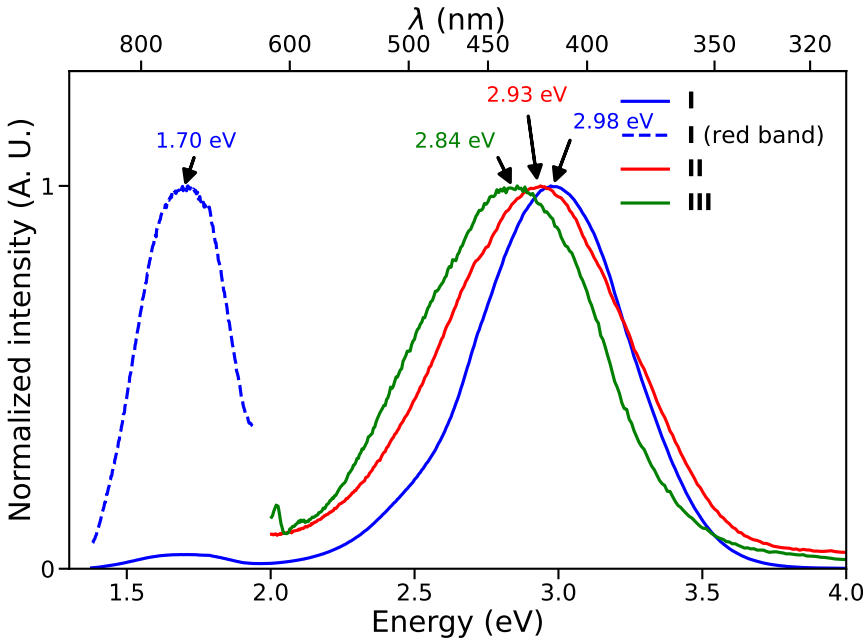

Figure 2: Recorded luminescence spectra of samples **I**, **II** and **III** at 300 K under excitation at 254 nm. The dotted line corresponds to the magnification of the blue line in the NIR-red region

Computed structure and electronic structure

α-Al_2O_3 crystallizes in the well-known corundum structure, where aluminum atoms are located in skewed octahedra (three short and three long Al–O distances).

In the first coordination sphere, each AlO_6 octahedron shares a triangular face with one other and three edges with three different octaheadra. In the second coordination sphere, each AlO_6 entity is surrounded by 6 corner shared octahedra. Oxygen atoms are located in tetrahedral sites. This arrangement is illustrated in Figure 3.

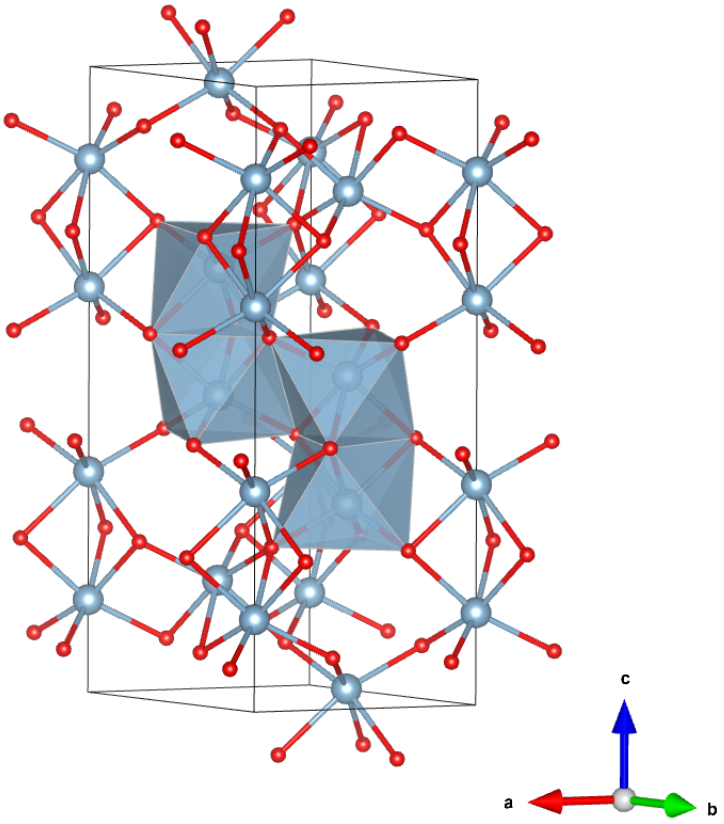

Figure 3: Conventional cell of α-Al_2O_3 with four octahedra represented to evidence the edge-sharing and face-sharing configurations. Blue and red spheres respectively represent Al and O atoms.

After relaxation of the pure (bulk) material, the a and c parameters are equal to 4.8063 and 13.1191 Å, and 4.7999 and 13.0418 Å, with the PBE (VASP) and PBE0 (CRYSTAL) functionals, respectively. Both are in good agreement with experiment (a = b = 4.7602(4)

Å, c = 12.9933(17) Å).[81] This good reproduction of the crystalline structure is of great importance to study afterwards the possible excited states, as well as the ground state vibrational properties.

On these grounds (point **A** of Figure 1), the Raman spectrum of the bulk system was simulated and compared with experiment (see SI). They are in excellent agreement in terms of band position. The normal modes at 379, 430, 449, 577, and 750 cm^{-1} are of E_g symmetry whereas the modes at 418 and 645 cm^{-1} correspond to the A_g ones.

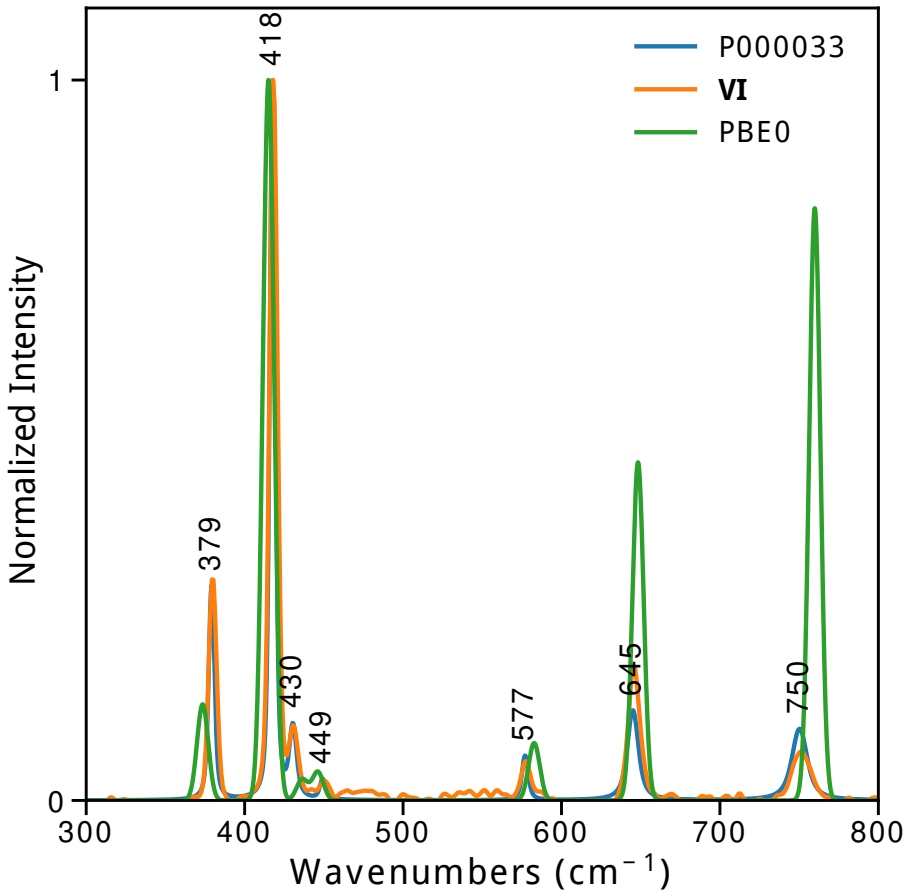

Figure 4: Experimental (P000033 sample in Ref.[82] in blue and ultrapure compound **VI** in orange) and simulated (green) Raman spectra of sapphire using the PBE0 functional and DZVP Rev2 basis.

Since the geometrical parameters of the ground state and the vibrational signatures are

accurately modeled, it is possible to investigate confidently the properties of the faulted material.

Simulation of the Ti^{3+} d–d transition

We first consider the point defect Ti_{Al}. In such a configuration, the Ti cation has undoubtfully the +III oxidation state (formally $3d^1$). The five d levels are found inside the bulk band gap. During the UV excitation process, an electron is promoted to an excited state that subsequently relaxes towards an empty Ti-d orbital. The expected deexcitation process corresponds to a d–d transition that triggers the red luminescence (namely $e_g \rightarrow t_{2g}$ electronic transition). After relaxing the excited states, the Vertical Transition energy (E_{Vertical}) was computed using the ΔSCF method. The simulated electronic emission is found around 770 nm (1.60 eV) which is very close to experiment (730 nm, 1.70 eV). The excellent agreement between simulation and experiment allows us to accurately describe the electronic transition (charge transfer). As one can see, the densities in the ground and excited states (**C** and **D** points respectively in Figure 1) are localized on the titanium and can be described as a combination of d orbitals (see Figure S2 in SI). Projections onto atomic orbitals show that they are a combination of d_{xy}, d_{yz} and d_{zx} in the GS and a combination of $d_{x^2-y^2}$ and d_{z^2} in the ES.

Thanks to the good reproduction of the luminescence properties, one can describe the structural modifications when going from R_G (A in Figure 1) to R_E (C in Figure 1). To that purpose, Ti–O distances are reported in the Table 2. As one can see, going from R_G to R_E, the largest Ti–O bond lengths have increased by 11% ($\approx$ 0.2 Å), while the smallest has decreased by 3%. This is the effect of the titanium atom moving away from its face sharing Al neighbor by 0.13 Å(Ti–Al interatomic distance 4.74% longer). Such a strong geometrical modification from the ground to the excited state has already been simulated in the case of ZrO_2:Ti.[58] This is associated to the occupancy of antibonding e_g level of titanium and depletion of the t_{2g} one.

Table 2: Defect–oxygen and defect–defect distances in computed structures for ground (R_G) and excited (R_E) states in the Ti_{Al} and the face-sharing Ti_{Al}+Mg_{Al} defects.

	R_G	R_E
Al_2O_3:Ti Ti–O (Å)	1.98×3, 2.09×3 (2.04)	1.92–2.32 (2.09)
Al_2O_3:Ti Ti–Al†(Å)	2.74	2.87
Al_2O_3:Ti,Mg Ti–O (Å)	1.94×3, 1.99×3 (1.96)	1.96–2.09 (2.03)
Al_2O_3:Ti,Mg Mg–O (Å)	1.94×3, 2.16×3 (2.05)	1.96×3, 2.13×3 (2.05)
Al_2O_3:Ti,Mg Ti–Mg (Å)	2.76	2.76

† Face sharing neighbor.

For each mode, the Franck-Condon shift $d^{\mathrm{FC}}_{G,i}$ is computed by the difference of potential energy between R_G and R_E projected on the direction of the mode. The Huang-Rhys factor S_i, is a dimensionless factor that characterizes vibronic coupling, is computed as the average number of vibrational quanta in the corresponding Franck-Condon shift. The mode specific Huang-Rhys factor shown as a function of the mode energy in Figure 5 is called the phonon spectral function. In this d–d transition, the defect-specific vibrational modes are found at the bottom of the energy range, in particular around 200 cm^{-1}. The mode around 200 cm^{-1} is strongly localized with a very low participation ratio ($p = 6\%$), and the main motion is the Ti^{3+} ion moving along its C_3 axis. On the other hand, higher energy modes are mostly collective motion from oxygen atoms and their contribution to the distortion is low.

Finally, electronic and vibrational contributions are combined into a vibronic spectrum. Figure 6 shows that it fits nicely the observed one. A band with a maximum around 1.60 eV is obtained, that is only 0.1 eV lower than the experiment. This slight underestimation is to be expected from a d–d transition in PBE and can be considered a very positive result. This demonstrates the strength of our computational protocol and allows us anticipating the luminescence band assignment in the blue region in the absence of fitting parameter.

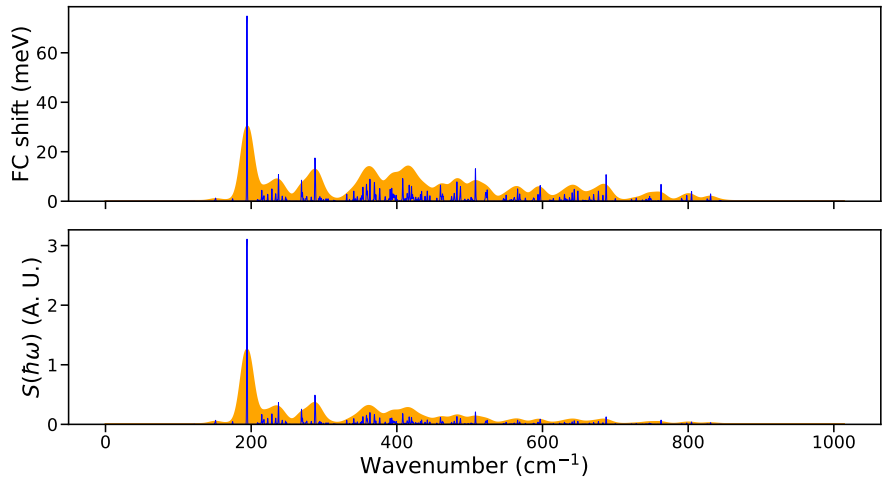

Figure 5: Phonon spectral function of the $Ti^{3+} \rightarrow Ti^{3+*}$ transition. For improved readability, an arbitrary Gaussian broadening with a standard deviation of 1 meV has been incorporated.

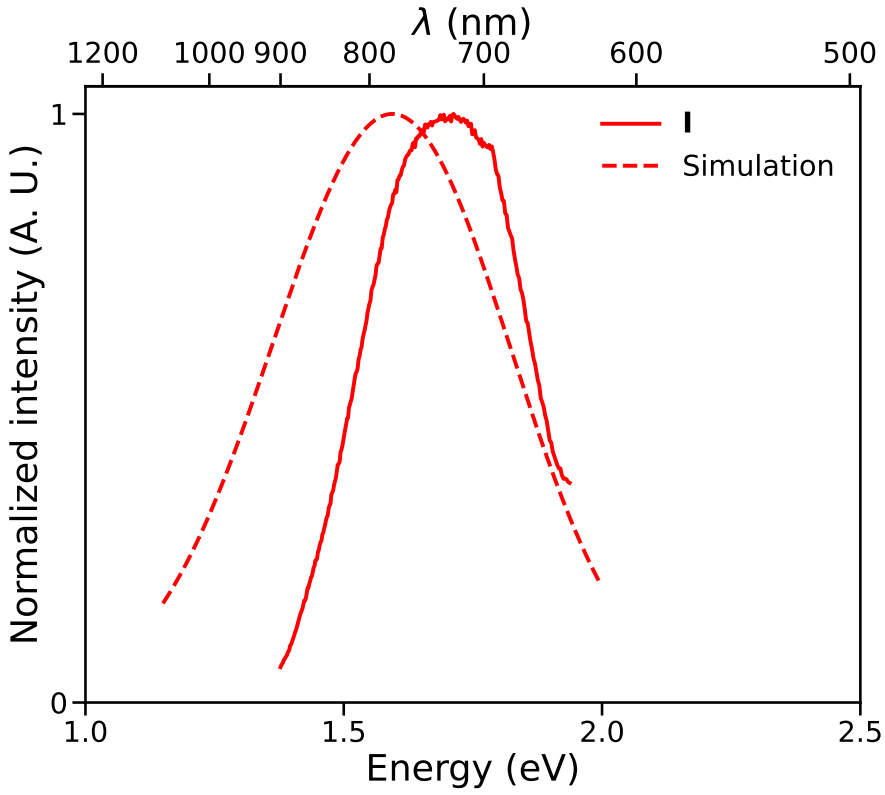

Figure 6: Experimental (solid) and simulated (dotted) luminescence spectra of the red band of **I** at 300 K. The FWHM is set to 0.6 eV.

Assignment of the blue luminescence

Based on the good agreement with experiment concerning the Ti^{3+} d-d transition, we used the same approach to determine the origin of the blue luminescence. Two main explanations for this luminescence arise from literature: (i) the presence of oxygen vacancies ($V_O^\times$), and (ii) a Ti–O charge transfer, involving the presence of Ti^{4+} cations at Al sites ($Ti_{Al}^\bullet$) concomitantly with countercations to balance the charge (*e.g.* X'_{Al}, X being a divalent cation).[27–31,37–43] To provide a definitive answer, we simulated both hypotheses.

Luminescence from an oxygen vacancy

For the simulation of luminescence due to oxygen vacancy, the same $2 \times 2 \times 1$ Al_2O_3 supercell was considered in which one of the oxygen atoms was removed. The atomic positions were then relaxed and the ground state structure ($V_O^\times$, neutral F center) attained. Indeed, the presence of the vacancy leads to the appearance of a doubly occupied localized level interspaced between the valence and the conduction bands. We noticed that the volume of the Al_4 tetrahedron surrounding the vacancy shrunk by 6% (from 2.98 Å^3 to 2.80 Å^3) compared to pristine Al_4O. The excited state was generated, after geometry optimization, by forcing the promotion of an electron of this localized state towards the conduction band. The charge density associated to this excited state (at the R_E position) is shown in Figure 7. The vacancy centered Al_4 inflated by 21% compared to the GS (from 2.80 Å^3 to 3.38 Å^3). The charge density isosurfaces, upon deexcitation, shows the disappearance of the nodal plane inside the vacancy, indicating a change of symmetry. To identify the nature of the phonons involved in the distortion, we look at the phonon spectral function in Figure 8a.

Three main contributions arise from (i) one localized mode (p = 14%) at 204 cm^{-1} concerning the four Al atoms around the vacancy; (ii) one delocalized mode (p = 42%) at 364 cm^{-1} corresponding to a bulk mode; (iii) a set of delocalized bulk modes (p from 35% to 70%) from 740 cm^{-1} to 840 cm^{-1}. Finally, the simulation of the optical spectrum is depicted in Figure 8b. The simulated spectrum exhibits a maximum at 445 nm (2.79 eV)

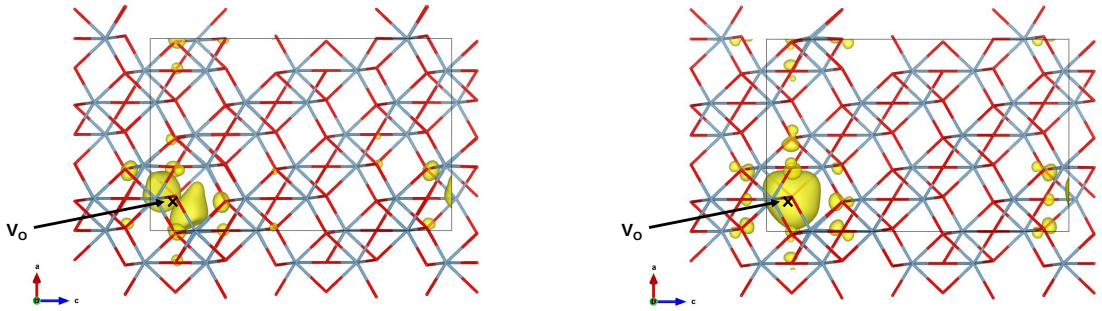

Figure 7: Charge density of frontier bands for Al_2O_3:V_O in yellow. Left: excited state (**C** point in Figure 1). Right: ground state (**D** point in Figure 1). Red and cyan nodes correspond to O and Al atoms, respectively.

and a FWHM of 0.72 eV.

Luminescence of Ti–O charge transfer

As stated before, to enable a +IV oxidation state for the titanium, the substitution of a second Al by a +II codopant is mandatory. Prior to our calculations, ICP-MS measurements (Table 1) were conducted on all the samples used in this study. They confirmed the presence of various +II impurities. In all natural compounds, the ICP-MS has found the presence of Mg. Therefore, we focused our attention on this codopant. We decided to investigate three positions of the +II cation relative to the Ti(+IV); *i.e.* face-sharing (FS), edge-sharing (ES), as well as "away"; *i.e.* as far as possible in the periodic supercell.

The introduction of these complex defects creates new unoccupied electronic levels in the gap of the material. These levels correspond to t_{2g} and e_g states from the Ti^{4+}. The expected transition is thus a charge transfer from one Ti state in the gap to the oxygen band.

Nevertheless, Table 3 clearly evidences that, according to the level of theory used in the present study, it is not possible to discriminate between edge-sharing and face-sharing configurations since both simulated energies are very close to experiment. However, it is clear that the distance between the cations may be a source of variation for the transition energy. For the rest of this section, we will focus on the face-sharing case for clarity.

Looking at the structural distortion (Table 2) in the excited state, one can see that the

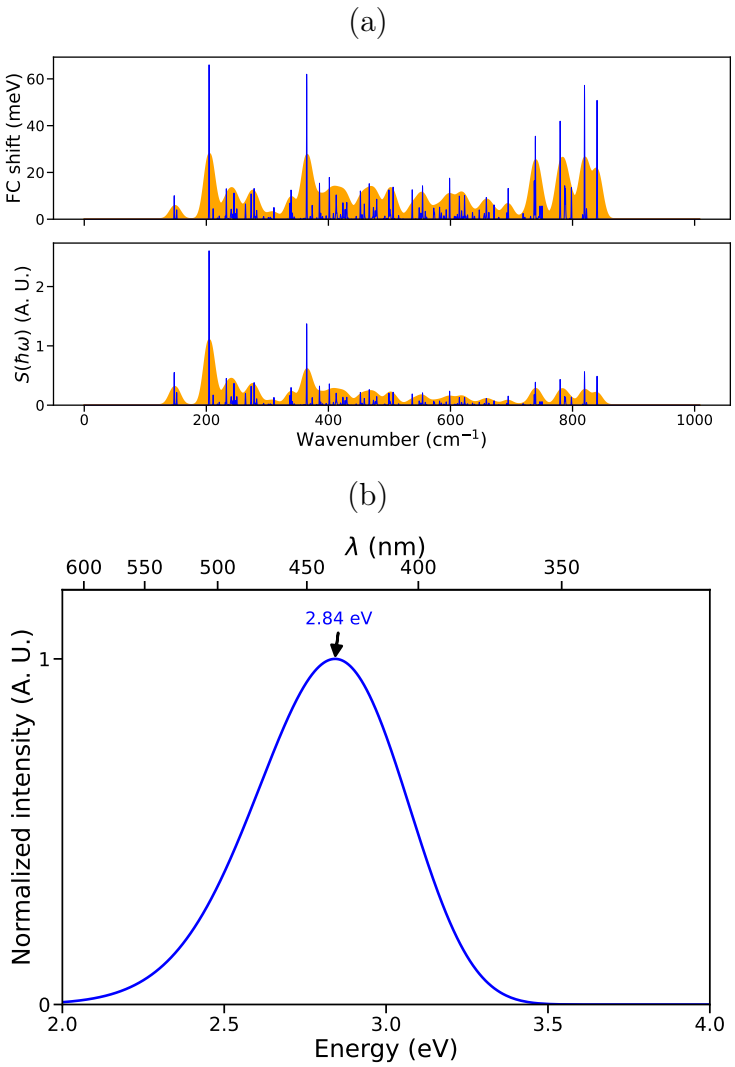

Figure 8: Phonon spectral function (a) and simulated luminescence spectrum (b) of Al_2O_3:V_O at 300 K.For (a), to improve readability, an arbitrary Gaussian broadening with a standard deviation of 1 meV has been incorporated. For (b), an the FWHM is set to 0.7 eV.

Ti–O bond lengths are the most affected ones; the longest Ti–O bond length increases by 5% (from 1.99 Å to 2.09 Å), while the Mg–O distances only slightly change (the longest distance only shrinking by 1.4%). In the face-sharing case, one can also note that the Ti–Mg distance does not vary significantly with the transition (staying at 2.76 Å).

We now discuss the charge transfer occurring in Al_2O_3:Ti,Mg. The charge densities in Figure 9 clearly show a charge transfer between a Ti-d orbital and O-p close to Mg. This result follows the ones obtained by our group for several oxides.[58,59]

Table 3: Experimental and simulated (electronic) luminescence wavelength/energy together with the computed Ti–Mg distance for the different cases dealing with the blue luminescence (Å).

		Emission (nm/eV)	Ti–Mg distance (Å)
Experiments	Trinkler *et al* (powder)[29]	417/2.98	—
	sample **I**	416/2.98	
	sample **II**	438/2.83	
	sample **III**	422/2.93	
Simulations	Al_2O_3:(Ti,Mg) (FS)	423/2.93†	2.76
	Al_2O_3:(Ti,Mg) (ES)	425/2.91†	2.85
	Al_2O_3:(Ti,Mg) ("away")	512/2.42†	8.10

† Vertical transition energies

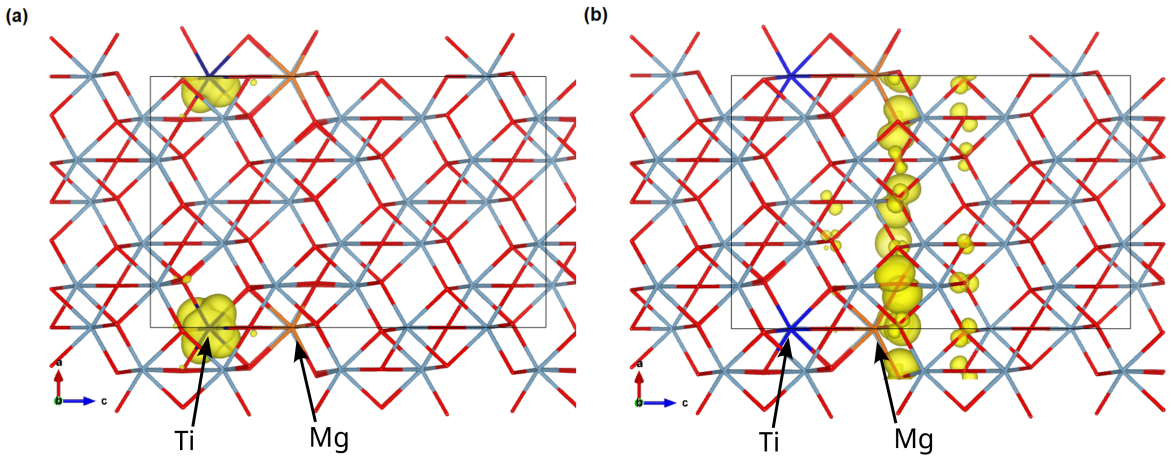

Figure 9: Charge density of frontier bands for Al_2O_3:(Ti,Mg) in yellow. Left: excited state (**C** point in Figure 1). Right: ground state (**D** point in Figure 1). Red, cyan, dark blue and orange sticks correspond to O, Al, Ti and Mg, respectively.

As shown by the phonon spectral function in Figure 10a the distortion is dominated by a set of delocalized ($p \geq 40\%$) modes from 750 to and 845 cm^{-1}. They correspond to bulk motions. The spectral functions for the edge-sharing case only marginally differ from the aforementioned one (see SI). In the "away" case, the same overall structure is found, with a more contrasted contribution of the higher energy modes and a larger total Huang-Rhys factor ($S_{\text{total}} = \sum_i S_i$).

Finally, the simulation of the luminescence spectrum of the Al_2O_3:Ti,Mg, showed in

Figure 10b produces bands that are centered around 3.02 eV, 2.98 eV and 2.60 eV for face-sharing, edge-sharing and away cases respectively.

Discussion

The simulations show a band around 2.87 eV for V_O and bands 3.02 eV, 2.98 eV and 2.60 eV for Ti,Mg FS, ES and "away", respectively. To identify the contribution of each transition in the observed luminescence bands, fits of a weighted sum of different theoretical transitions are performed. Moreover, the FS and ES transitions are too close to be distinguished. Consequently, the ES contribution is excluded in the summation leaving Ti,Mg FS, Ti,Mg "away" and V_O transitions for the band assignment. In all the fits, the same individual bands are used with only a weight prefactor. The result of these optimizations are displayed in Figure 11. Interestingly, it shows that the sample **I** exhibits mostly Ti,Mg FS luminescence, with a small contribution of V_O. It is to be noticed that **I** show that the width predicted in this approach is probably slightly overestimated, preventing as good a fit as for the other samples. The sample **II** sample shows similar results, with a small added contribution of the Ti,Mg away spectrum. Finally, the luminescence of sample **III** can mostly be explained by vacancies, with a small contribution of Ti,Mg away. As one can see, in the absence of any fitting parameters except for the relative importance of each transition, the simulated spectra fit nicely experiment.

Towards a predictive model

On these grounds, the predictive capability of our methodology was tested. To do so, only the luminescence spectra of Ti,Ca FS and Ti,Be FS were simulated in a similar way to Mg. For long Ti–M distances, no effect of the nature of the codoping cation is expected on the luminescence as only the long-distance coulombic interaction remains. As a consequence, for the new cations, only the FS configurations have been considered. The Ti,Ca model predicts a large band centered around 2.70 eV (FWHM = 0.84 eV) while the Ti,Be one yields a

similarly large band centered around 3.24 eV (FWHM = 0.75 eV). The photoluminescence of the beryllium-diffused material (sample **V**) together with the syntheses of Al_2O_3 codoped with Ti,Ca (sample **IV**) were recorded. Since the ICP-MS (Table 1) shows the presence of Mg and Ca in both samples, the decompositions of both spectra included the simulated Ti,Mg (FS) and Ti,Ca (FS) spectra.

The Ti,Be spectrum was also used in the decomposition of the sample **V**. The results of these decompositions are shown in Figure 12.

The sample **V** shows no contribution of the Be related band. Instead, we find a contribution of the vacancies that can be compared with the other natural sample (**II**) as well as significant contributions of Mg and Ca related bands, as expected from the ICP-MS.

The sample **IV** shows a large contribution of vacancies, like the other powder (**III**), as well as a significant contribution of the Ca band. The Ti,Mg band is also present.

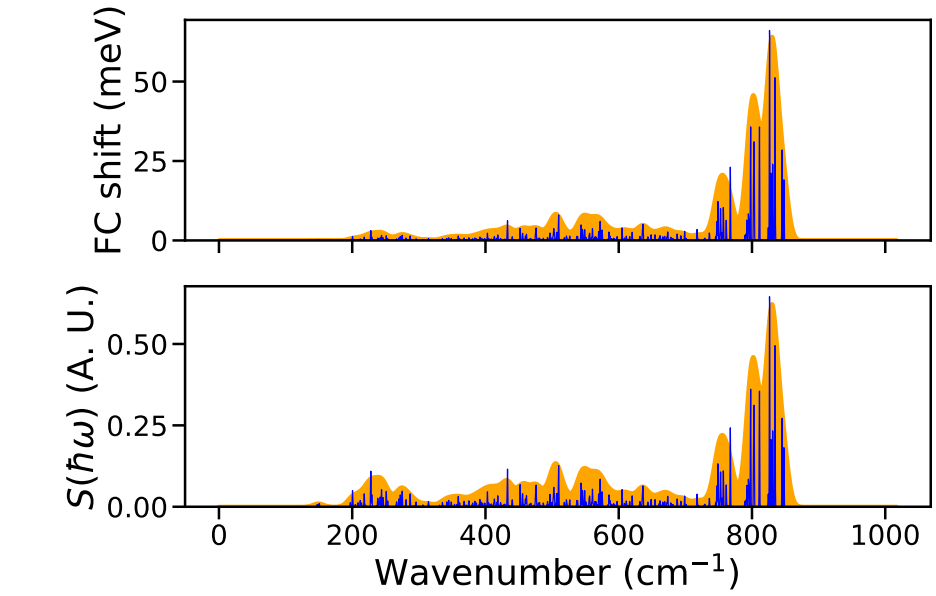

(a)

(b)

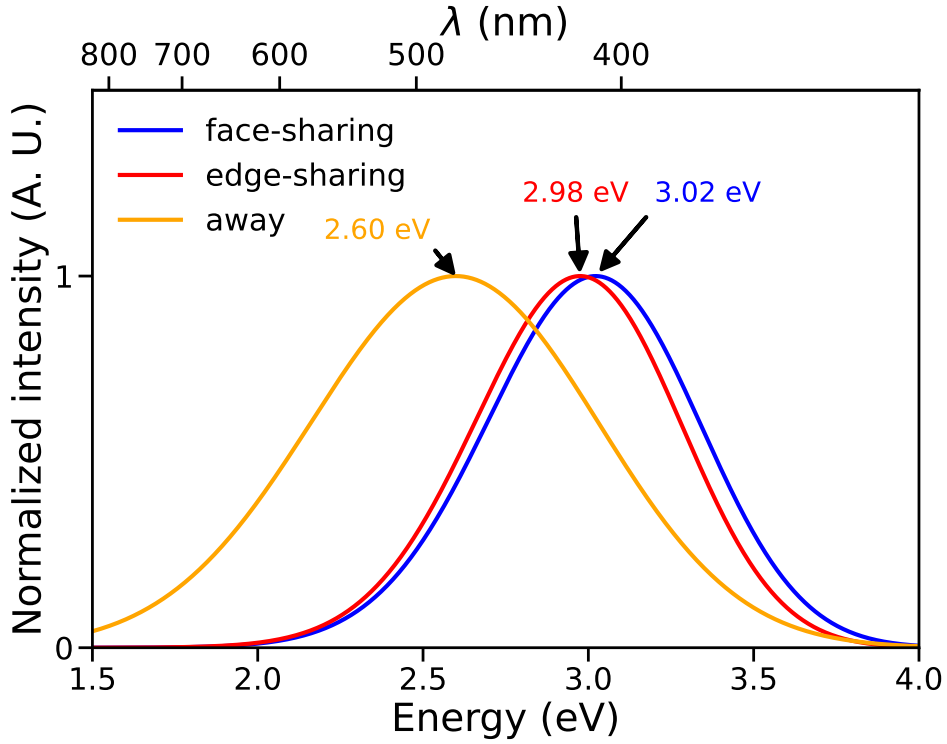

Figure 10: Phonon spectral function (a) for the FS Ti,Mg transition and (b) comparison of the three cases of Ti,Mg spectra simulations at 300 K. The band FWHM are 0.66 eV, 0.66 eV, and 0.82 eV respectively. For (a), to improve readability, an arbitrary Gaussian broadening with a standard deviation of 1 meV has been incorporated. For (b), an the FWHM were set 0.66, 0.66 and 0.82 eV for the curves in blue, red and orange, respectively.

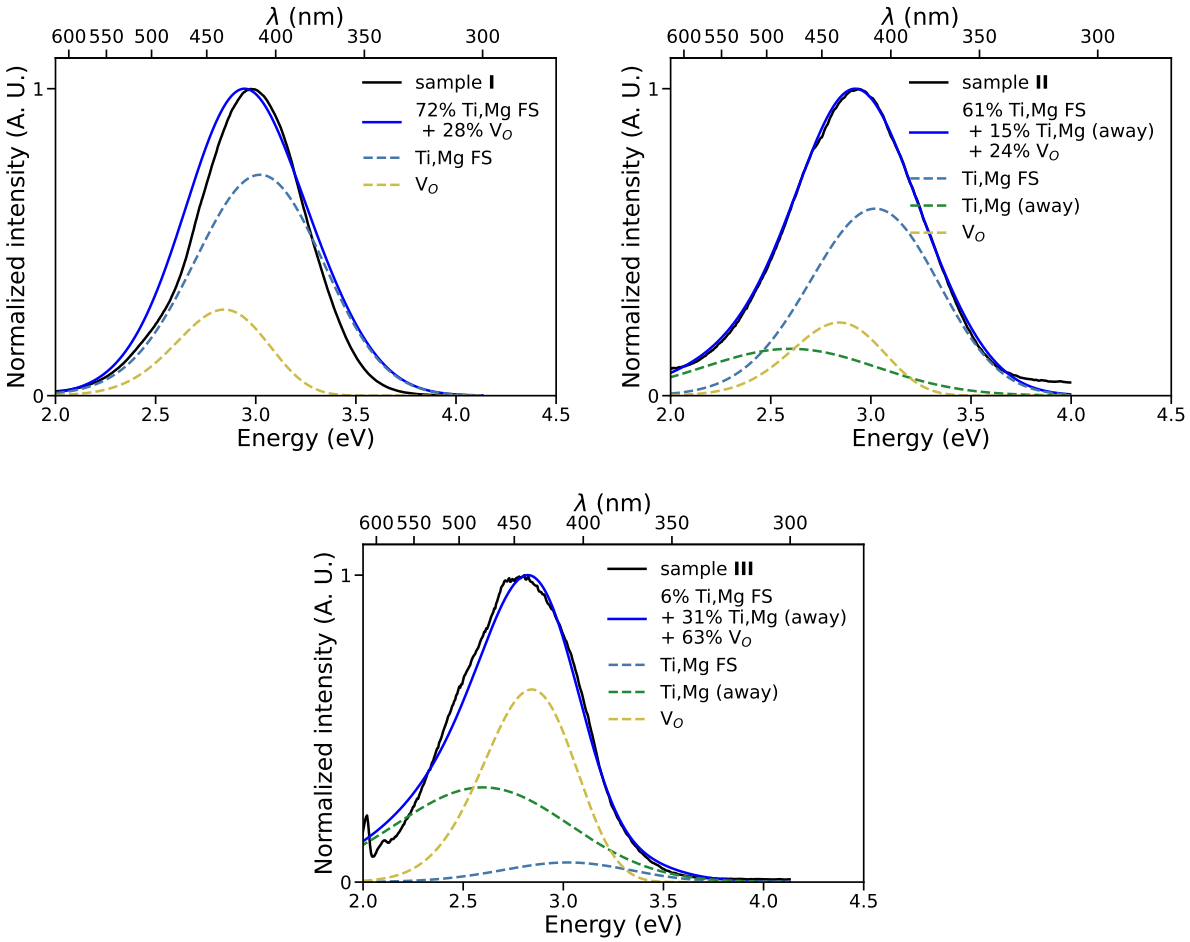

Figure 11: Results of fitting the experimental spectra with a combination of V_O and Ti,Mg spectra.

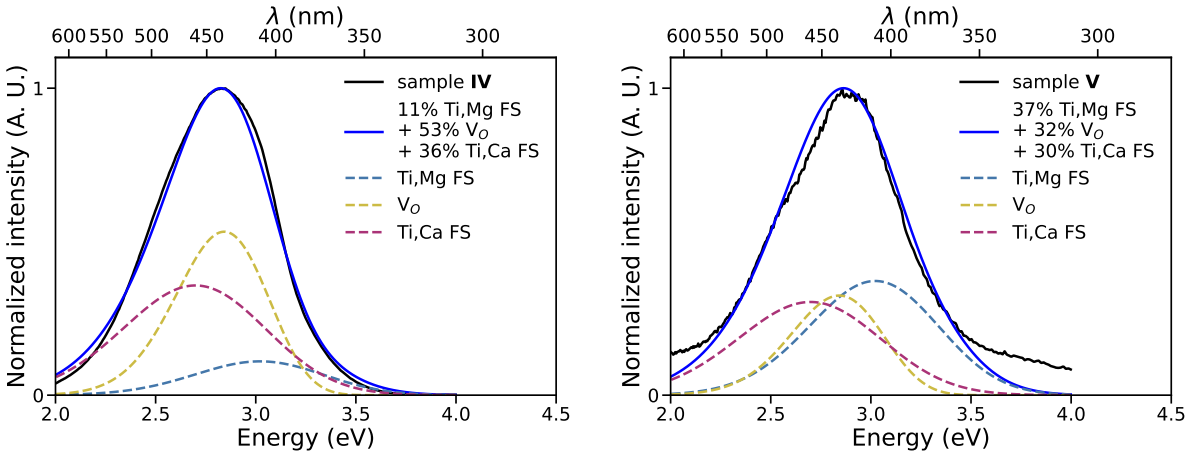

Figure 12: Decomposition of the luminescence of samples **IV** and **V** into the simulated spectra.

CIE(x, y) diagrams

We would now be able to simulate the color of the samples luminescence. We used all the fitted compositions and the corresponding samples and computed chromaticity coordinates from the spectra. For the sample **I**, we also added the red band associated with Ti^{3+} to the composition of the spectrum. As absolute intensities are not yet available in our simulation protocol, we used the relative intensity between the two experimental bands of 1:27 to combine the simulated bands.

The results are provided in a CIE chromaticity diagram in Figure 13. Coordinates of all the points are detailed in SI. As one can see the reproduction of colors is very accurate.

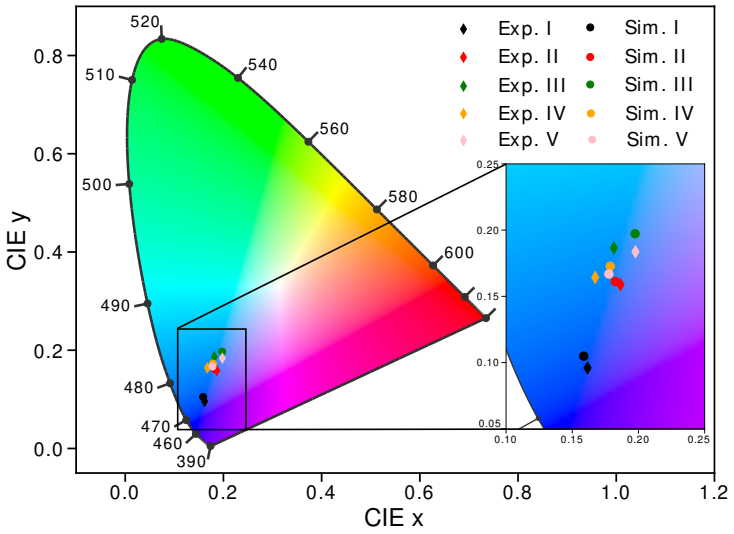

Figure 13: CIE chromaticity diagram for all samples and their associated simulations.

Conclusion

In this paper, we demonstrated that we are able to accurately simulate the luminescence spectra of Al_2O_3:Ti for various compositions. First, we were able to reproduce the well-known red luminescence of the Ti^{3+} d-d transition and the charge density confirms our capability to deal with d^1 transition.

Second, we were able to show that the blue luminescence results from several processes including both the oxygen vacancies and the possible presence of a Ti,M codoping. Our model unambiguously reproduces the blue band with a high accuracy.

Finally, the simulated CIE chromaticity diagrams agree with the experiment.

These results based on parameter-free method open new possibilities for experimentally and theoretically oriented chemists to interact, since we can now successfully simulate excited state properties.

Acknowledgement

This work was granted access to the HPC resources of TGCC under allocation A0100912471 and A0120913422 made by GENCI. CL and TC particularly thank the financial support by the ANR MoRDOR project of the French National Research Agency and the CNRS. We thank Elodie Grange for the synthesis of doped Al_2O_3 powders D and E. Daniel Ritz is deeply acknowledged for the ultrapure alumina sample loan as well as Carole La on the implementation of the measures by LA-ICP-MS.

Supporting Information Available

- Details of atomic distances in Al_2O_3:Ti and Al_2O_3:Ti,Mg;
- Charge density representation of frontier bands in Al_2O_3:Ti in ground an excited state;
- Projected density of state of ground state Al_2O_3:Ti,Be, Al_2O_3:Ti,Mg, and Al_2O_3:Ti,Ca;
- XRD patterns of synthesized samples **III** and **IV**;
- Bandwidth approximation from ES PES;
- Synthesis protocol;
- Experimental and Simulated CIE coordinates

References

(1) Pines, H.; Haag, W. O. Alumina: catalyst and support. I. alumina, its intrinsic acidity and catalytic activity1. *Journal of the American Chemical Society* **1960**, *82*, 2471–2483.

(2) Akselrod, M.; Kortov, V.; Kravetsky, D.; Gotlib, V. Highly sensitive thermoluminescent anion-defective α-Al_2O_3: C single crystal detectors. *Radiation Protection Dosimetry* **1990**, *32*, 15–20.

(3) Auerkari, P. *Mechanical and physical properties of engineering alumina ceramics*; Technical Research Centre of Finland Espoo, 1996; Vol. 23; pp 1–26.

(4) Myung, S.-T.; Izumi, K.; Komaba, S.; Sun, Y.-K.; Yashiro, H.; Kumagai, N. Role of alumina coating on Li- Ni- Co- Mn- O particles as positive electrode material for lithium-ion batteries. *Chemistry of Materials* **2005**, *17*, 3695–3704.

(5) Trueba, M.; Trasatti, S. P. γ-Alumina as a support for catalysts: a review of fundamental aspects. *European Journal of Inorganic Chemistry* **2005**, *2005*, 3393–3403.

(6) Dobrovinskaya, E. R.; Lytvynov, L. A.; Pishchik, V. *Sapphire: material, manufacturing, applications*; Springer Science & Business Media, 2009.

(7) Lu, X.; Xia, G.; Lemmon, J. P.; Yang, Z. Advanced materials for sodium-beta alumina batteries: Status, challenges and perspectives. *Journal of Power Sources* **2010**, *195*, 2431–2442.

(8) Ekendahl, D.; Judas, L. Retrospective dosimetry with alumina substrate from electronic components. *Radiation Protection Dosimetry* **2012**, *150*, 134–141.

(9) Woo, J. H.; Travis, J. J.; George, S. M.; Lee, S.-H. Utilization of Al_2O_3 atomic layer deposition for Li ion pathways in solid state Li batteries. *Journal of The Electrochemical Society* **2014**, *162*, A344.

(10) Dingemans, G.; Kessels, W. Status and prospects of Al_2O_3-based surface passivation schemes for silicon solar cells. *Journal of Vacuum Science & Technology A: Vacuum, Surfaces, and Films* **2012**, *30*, 040802.

(11) Al-Sanabani, F. A.; Madfa, A. A.; Al-Qudaimi, N. H. Alumina ceramic for dental applications: A review article. *American Journal of Materials Research* **2014**, *1*, 26–34.

(12) Busca, G. Silica-alumina catalytic materials: A critical review. *Catalysis Today* **2020**, *357*, 621–629.

(13) Dubinsky, E. V.; Stone-Sundberg, J.; Emmett, J. L. A quantitative description of the causes of color in corundum. *Gems & Gemology* **2020**, *56*, 1–27.

(14) Ferguson, J.; Fielding, P. The origins of the colours of yellow, green and blue sapphires. *Chemical Physics Letters* **1971**, *10*, 262–265.

(15) Sugano, S.; Tanabe, Y. Absorption spectra of Cr3+ in Al2O3 part A. Theoretical studies of the absorption bands and lines. *Journal of the Physical Society of Japan* **1958**, *13*, 880–899.

(16) Kvapil, J.; Súlovskỳ, J.; Kvapil, J.; Perner, B. The influence of dopants and annealing on the colour stability of ruby. *physica status solidi (a)* **1972**, *9*, 665–672.

(17) Kulinkin, A.; Feofilov, S.; Zakharchenya, R. Luminescence of impurity 3 d and 4 f metal ions in different crystalline forms of Al 2 O 3. *Physics of the Solid State* **2000**, *42*, 857–860.

(18) Nassau, K. Heat treating ruby and sapphire: technical aspects. *Gems & Gemology* **1981**, *17*, 121–131.

(19) Nikolskaya, L.; Terekhova, V.; Samoilovich, M. On the origin of natural sapphire color. *Physics and Chemistry of Minerals* **1978**, *3*, 213–224.

(20) Sibbett, W.; Lagatsky, A.; Brown, C. The development and application of femtosecond laser systems. *Optics Express* **2012**, *20*, 6989–7001.

(21) Moulton, P. Ti-doped sapphire: tunable solid-state laser. *Optics News* **1982**, *8*, 9–9.

(22) Winkler, E.; Sarver, J.; Cutler, I. B. Solid solution of titanium dioxide in aluminum oxide. *Journal of the American Ceramic Society* **1966**, *49*, 634–637.

(23) Macfarlane, R.; Wong, J.; Sturge, M. Dynamic Jahn-Teller effect in octahedrally coordinated d^1 impurity systems. *Physical Review* **1968**, *166*, 250.

(24) Gächter, B.; Koningstein, J. Zero phonon transitions and interacting Jahn-Teller phonon energies from the fluorescence spectrum of α-Al_2O_3: Ti^{3+}. *The Journal of Chemical Physics* **1974**, *60*, 2003–2006.

(25) Draeger, B.; Summers, G. Defects in unirradiated α-Al_2O_3. *Physical Review B* **1979**, *19*, 1172.

(26) Summers, G. Thermoluminescence in single crystal α-Al_2O_3. *Radiation Protection Dosimetry* **1984**, *8*, 69–80.

(27) Lacovara, P.; Esterowitz, L.; Kokta, M. Growth, spectroscopy, and lasing of titanium-doped sapphire. *IEEE Journal of Quantum Electronics* **1985**, *21*, 1614–1618.

(28) Chen, W.; Tang, H.; Shi, C.; Deng, J.; Shi, J.; Zhou, Y.; Xia, S.; Wang, Y.; Yin, S. Investigation on the origin of the blue emission in titanium doped sapphire: Is F^+ color center the blue emission center ? *Applied Physics Letters* **1995**, *67*, 317–319.

(29) Trinkler, L.; Berzina, B.; Jakimovica, D.; Grabis, J.; Steins, I. Peculiarities of photoluminescence of Al2O3 bulk and nanosize powders at low temperatures. *Optical Materials* **2011**, *33*, 817–822.

(30) Perevalov, T.; Tereshenko, O.; Gritsenko, V.; Pustovarov, V.; Yelisseyev, A.; Park, C.; Han, J. H.; Lee, C. Oxygen deficiency defects in amorphous Al_2O_3. *Journal of Applied Physics* **2010**, *108*, 013501.

(31) Mikhailik, V.; Di Stefano, P.; Henry, S.; Kraus, H.; Lynch, A.; Tsybulskyi, V.; Verdier, M. Studies of concentration dependences in the luminescence of Ti-doped Al_2O_3. *Journal of Applied Physics* **2011**, *109*, 053116.

(32) Zorenko, Y.; Zorenko, T.; Voznyak, T.; Nizhankovskiy, S.; Krivonosov, E.; Danko, A.; Puzikov, V. Comparative study of the luminescence of Al_2O_3:Ti and Al_2O_3 crystals under VUV synchrotron radiation excitation. *Optical Materials* **2013**, *35*, 2053–2055.

(33) Zhou, D.; Xia, C.; Guyot, Y.; Zhong, J.; Xu, X.; Feng, S.; Lu, W.; Song, J.; Lebbou, K. Growth and spectroscopic properties of Ti-doped sapphire single-crystal fibers. *Optical Materials* **2015**, *47*, 495–500.

(34) Alombert-Goget, G.; Li, H.; Guyot, Y.; Brenier, A.; Lebbou, K. Luminescence and coloration of undoped and Ti-doped sapphire crystals grown by Czochralski technique. *Journal of Luminescence* **2016**, *169*, 516–519.

(35) Powell, R. C.; Venikouas, G. E.; Xi, L.; Tyminski, J. K.; Kokta, M. R. Thermal effects on the optical spectra of Al_2O_3: Ti^{3+}. *The Journal of Chemical Physics* **1986**, *84*, 662–665.

(36) Reisfeld, R.; Eyal, M.; Jorgensen, C. K. Unusual luminescence of titanium (III) in aluminium-oxide. *Chimia* **1987**, *41*, 117–119.

(37) Blasse, G.; Verweij, J. The luminescence of titanium in sapphire laser material. *Materials Chemistry and Physics* **1990**, *26*, 131–137.

(38) Evans, B. D. Ubiquitous blue luminescence from undoped synthetic sapphires. *Journal of Luminescence* **1994**, *60*, 620–626.

(39) Ruza, E.; Reyher, H.; Trokss, J.; Wöhlecke, M. Optically detected magnetic resonance studied via the blue luminescence of Ti-doped. *Journal of Physics: Condensed Matter* **1998**, *10*, 4297.

(40) Akselrod, M. S.; Akselrod, A. E. New Al_2O_3: C, Mg crystals for radiophotoluminescent dosimetry and optical imaging. *Radiation Protection Dosimetry* **2006**, *119*, 218–221.

(41) Page, P.; Dhabekar, B.; Bhatt, B.; Dhoble, A.; Godbole, S. Role of Ti^{4+} in the luminescence process of Al_2O_3: Si, Ti. *Journal of Luminescence* **2010**, *130*, 882–887.

(42) Macalik, B.; Bausa, L.; Garcia-Sole, J.; Jaque, F.; Munoz Santiuste, J.; Vergara, I. Blue emission in Ti-sapphire laser crystals. *Applied Physics A* **1992**, *55*, 144–147.

(43) Bausa, L.; Vergara, I.; Jaque, F.; Sole, J. G. Ultraviolet laser excited luminescence of Ti-sapphire. *Journal of Physics: Condensed Matter* **1990**, *2*, 9919.

(44) Chapoulie, R.; Capdupuy, C.; Schvoerer, M.; Bechtel, F. Cathodoluminescence and crystal growth of sapphire. *physica status solidi (a)* **1999**, *171*, 613–621.

(45) Vigier, M.; Fritsch, E.; Cavignac, T.; Latouche, C.; Jobic, S. Shortwave UV Blue Luminescence of Some Minerals and Gems Due to Titanate Groups. *Minerals* **2023**, *13*, 104.

(46) Carrasco, J.; Lopez, N.; Sousa, C.; Illas, F. First-principles study of the optical transitions of F centers in the bulk and on the (0001) surface of α-Al_2O_3. *Physical Review B* **2005**, *72*, 054109.

(47) Stoliaroff, A.; Latouche, C.; Jobic, S. Versatile electrical behavior of $1T-TiS_2$ elucidated from a theoretical study. *Physical Review B* **2019**, *99*, 165122.

(48) Watcharatharapong, T.; T-Thienprasert, J.; Limpijumnong, S. Theoretical study of optical properties of native point defects in α-Al_2O_3. *Integrated Ferroelectrics* **2014**, *156*, 79–85.

(49) Xiang, X.; Zhang, G.; Yang, F.; Peng, X.; Tang, T.; Shi, Y.; Wang, X. An insight to the role of Cr in the process of intrinsic point defects in α-Al_2O_3. *Physical Chemistry Chemical Physics* **2016**, *18*, 6734–6741.

(50) Kravchenko, L. Y.; Fil, D. Defect complexes in Ti-doped sapphire: A first principles study. *Journal of Applied Physics* **2018**, *123*, 023104.

(51) Futazuka, T.; Ishikawa, R.; Shibata, N.; Ikuhara, Y. First-principles calculations of group IIA and group IV impurities in α-Al_2O_3. *Physical Review Materials* **2020**, *4*, 073602.

(52) Hu, X.-K.; Wu, B.; Yang, Y.; Yeung, Y. Y.; Ma, C.-G.; Brik, M. An old system revisited: Al_2O_3: Ti^{3+}-microscopic crystal field effects explored by the crystal field and first-principles calculations. *Journal of Alloys and Compounds* **2020**, *847*, 156459.

(53) Kravchenko, L. Y.; Fil, D. Control of charge state of dopants in insulating crystals: Case study of Ti-doped sapphire. *Physical Review Research* **2020**, *2*, 023135.

(54) Gong, Q.; Zhao, C.; Li, S.; Zhao, G.; Xu, M.; Hang, Y. Theoretical study on near UV and visible optical absorption characteristics of Ti-doped α-Al_2O_3 single crystals. *Materials Today Communications* **2021**, *28*, 102506.

(55) Jing, W.; Liu, M.; Wen, J.; Ning, L.; Yin, M.; Duan, C.-K. First-principles study of Ti-doped sapphire. I. Formation and optical transition properties of titanium pairs. *Physical Review B* **2021**, *104*, 165103.

(56) Jing, W.; Liu, M.; Wen, J.; Ning, L.; Yin, M.; Duan, C.-K. First-principles study of Ti-doped sapphire. II. Formation and reduction of complex defects. *Physical Review B* **2021**, *104*, 165104.

(57) Palakawong, N.; Sukharom, S.; Limpijumnong, S.; Jungthawan, S.; Limkumnerd, S.; Boonchun, A.; Reunchan, P.; T-Thienprasert, J. Hybrid-Functional Study of Native

Point Defects and Ti/Fe Impurities in α-Al_2O_3. *physica status solidi (b)* **2021**, *258*, 2000498.

(58) Lafargue-Dit-Hauret, W.; Schira, R.; Latouche, C.; Jobic, S. Theoretical Calculations Meet Experiment to Explain the Luminescence Properties and the Presence of Defects in m-ZrO_2. *Chemistry of Materials* **2021**, *33*, 2984–2992.

(59) Cavignac, T.; Jobic, S.; Latouche, C. Modeling Luminescence Spectrum of $BaZrO_3$: Ti Including Vibronic Coupling from First Principles Calculations. *Journal of Chemical Theory and Computation* **2022**, *18*, 7714–7721.

(60) Emmett, J. L.; Scarratt, K.; McClure, S. F.; Moses, T.; Douthit, T. R.; Hughes, R.; Novak, S.; Shigley, J. E.; Wang, W.; Bordelon, O.; others Beryllium diffusion of ruby and sapphire. *Gems & Gemology* **2003**, *39*, 84–135.

(61) Kresse, G.; Furthmüller, J. Efficiency of Ab-Initio Total Energy Calculations for Metals and Semiconductors Using a Plane-Wave Basis Set. *Computational Materials Science* **1996**, *6*, 15.

(62) Kresse, G.; Furthmüller, J. Efficient Iterative Schemes for Ab Initio Total-Energy Calculations Using a Plane-Wave Basis Set. *Physical Review B: Condensed Matter* **1996**, *54*, 11169.

(63) Perdew, J. P.; Burke, K.; Ernzerhof, M. Generalized Gradient Approximation Made Simple. *Physical Review Letters* **1996**, *77*, 3865–3868.

(64) Kresse, G.; Joubert, D. From Ultrasoft Pseudopotentials to the Projector Augmented-Wave Method. *Physical Review B: Condensed Matter* **1999**, *59*, 1758.

(65) Dovesi, R.; Erba, A.; Orlando, R.; Zicovich-Wilson, C. M.; Civalleri, B.; Maschio, L.; Rérat, M.; Casassa, S.; Baima, J.; Salustro, S.; Kirtman, B. Quantum-mechanical con-

densed matter simulations with CRYSTAL. *WIREs Computational Molecular Science* **2018**, *8*, 1–36.

(66) Adamo, C.; Barone, V. Toward reliable density functional methods without adjustable parameters: The PBE0 model. *The Journal of Chemical Physics* **1999**, *110*, 6158–6170.

(67) Oliveira, D. V.; Laun, J.; Peintinger, M. F.; Bredow, T. BSSE-correction scheme for consistent gaussian basis sets of double- and triple-zeta valence with polarization quality for solid-state calculations. *Journal of Computational Chemistry* **2019**, *40*, 2364–2376.

(68) Schira, R.; Latouche, C. DFT vs. TDDFT vs. TDA to simulate phosphorescence spectra of Pt- and Ir-based complexes. *Dalton Transaction* **2021**, *50*, 746–753.

(69) Martìnez-Vollbert, E.; Ciambrone, C.; Lafargue-Dit-Hauret, W.; Latouche, C.; Loiseau, F.; Lanoë, P.-H. Bis-Heteroleptic Cationic Iridium (III) Complexes Featuring Cyclometalating 2-Phenylbenzimidazole Ligands: A Combined Experimental and Theoretical Study. *Inorganic Chemistry* **2022**, *61*, 3033–3049.

(70) Utrera-Melero, R.; Huitorel, B.; Cordier, M.; Massuyeau, F.; Mevellec, J.-Y.; Stephant, N.; Deniard, P.; Latouche, C.; Martineau-Corcos, C.; Perruchas, S. Mechanically responsive luminescent films based on copper iodide clusters. *Journal of Materials Chemistry C* **2021**, *9*, 7991–8001.

(71) Barone, V.; Baiardi, A.; Biczysko, M.; Bloino, J.; Cappelli, C.; Lipparini, F. Implementation and validation of a multi-purpose virtual spectrometer for large systems in complex environments. *Physical Chemistry Chemical Physics* **2012**, *14*, 12404–12422.

(72) Baiardi, A.; Bloino, J.; Barone, V. General time dependent approach to vibronic spectroscopy including Franck–Condon, Herzberg–Teller, and Duschinsky effects. *Journal of chemical theory and computation* **2013**, *9*, 4097–4115.

(73) Adamo, C.; Jacquemin, D. The calculations of excited-state properties with Time-Dependent Density Functional Theory. *Chemical Society Reviews* **2013**, *42*, 845–856.

(74) Jacquemin, D.; Mennucci, B.; Adamo, C. Excited-state calculations with TD-DFT: from benchmarks to simulations in complex environments. *Physical Chemistry Chemical Physics* **2011**, *13*, 16987–16998.

(75) Lax, M. The Franck-Condon Principle and Its Application to Crystals. *The Journal of Chemical Physics* **1952**, *20*, 1752–1760.

(76) Kubo, R.; Toyozawa, Y. Application of the Method of Generating Function to Radiative and Non-Radiative Transitions of a Trapped Electron in a Crystal. *Progress of Theoretical Physics* **1955**, *13*, 160–182.

(77) Henderson, B.; Imbusch, G. F. *Optical Spectroscopy of Inorganic Solids*; Monographs on the Physics and Chemistry of Materials; Oxford University Press: Oxford, New York, 2006; Chapter 5.

(78) *Optical Spectroscopy of Inorganic Solids*; Monographs on the Physics and Chemistry of Materials; Oxford University Press: Oxford, New York, 2006; pp 183–220.

(79) Pascale, F.; Zicovich-Wilson, C. M.; López Gejo, F.; Civalleri, B.; Orlando, R.; Dovesi, R. The calculation of the vibrational frequencies of crystalline compounds and its implementation in the CRYSTAL code. *Journal of Computational Chemistry* **2004**, *25*, 888–897.

(80) Bell, R. J.; Dean, P.; Hibbins-Butler, D. C. Localization of normal modes in vitreous silica, germania and beryllium fluoride. *Journal of Physics C: Solid State Physics* **1970**, *3*, 2111–2118.

(81) Lewis, J.; Schwarzenbach, D.; Flack, H. D. Electric field gradients and charge density in corundum, α-Al2O3. *Acta Crystallographica Section A: Crystal Physics, Diffraction,*

Theoretical and General Crystallography **1982**, *38*, 733–739, Number: 5 Publisher: International Union of Crystallography.

(82) rruff database: Al2O3. 2022; `https://rruff.info/P000033`, Last visite: 04/25/2022.